Unleashing Giant Förster Resonance Energy Transfer by Bound State in the Continuum

Zhiyi Yuan, Ningyuan Nie, Yuhao Wang, Thi Thu Ha Do, Vytautas Valuckas, Christian Seassal, Yu-Cheng Chen, Hai Son Nguyen, Son Tung Ha, Cuong Dang

Unleashing Giant Förster Resonance Energy Transfer by Bound State in The Continuum

Zhiyi Yuan[1,2,3], Ningyuan Nie[1], Yuhao Wang[1], Thi Thu Ha Do[3], Vytautas Valuckas[3], Christian Seassal[4], Yu-Cheng Chen[1], Hai Son Nguyen[4,5], Son Tung Ha[3,*], Cuong Dang[1,2*]

[1] Centre for OptoElectronics and Biophotonics (COEB), School of Electrical and Electronic Engineering, Nanyang Technological University, Singapore 639798

[2] CNRS-International-NTU-Thales Research Alliance (CINTRA), IRL 3288, Singapore 637553

[3] Institute of Materials Research and Engineering, Agency for Science Technology and Research (A*STAR), 2 Fusionopolis Way, Singapore 138634

[4] Univ Lyon, Ecole Centrale de Lyon, CNRS, INSA Lyon, Universite Claude Bernard Lyon 1, CPE Lyon, CNRS, INL, UMR5270, 69130 Ecully, France

[5] Institut Universitaire de France (IUF), F-75231 Paris, France

*Corresponding authors: Son Tung Ha: ha_son_tung@imre.a-star.edu.sg & Cuong Dang: hcdang@ntu.edu.sg

Abstract: Förster resonance energy transfer (FRET), driven by dipole-dipole interactions (DDIs), is widely utilized in chemistry, biology, and nanophotonics. However, conventional FRET is ineffective at donor-acceptor distances exceeding 10 nm, and measurements suffer from low signal-to-noise ratios. In this study, we demonstrate significant FRET enhancement and extended interaction distances under ambient conditions by utilizing a bound state in the continuum (BIC) mode within a dielectric metasurface cavity. This enhancement is achieved by leveraging the ultrahigh quality factors, minimal material absorption, and non-local effects associated with the BIC mode. Spectrally and angularly resolved photoluminescence (PL) lifetime measurements reveal that the BIC mode significantly increases FRET rate and interaction distance. The FRET rate is enhanced by up to 70-fold, and the interaction distance is significantly boosted by over an order of magnitude, reaching ~100 nm. These findings offer valuable insights for achieving long-range, high-efficiency FRET and collective DDIs using loss-less dielectric metasurfaces.

Keywords: Förster resonance energy transfer (FRET), bound state in the continuum, Titanium dioxide, Purcell effect, dipole-dipole interaction, dielectric metasurface.

Dipole-dipole interactions (DDIs) are fundamental to light-matter interaction, playing a crucial role in phenomena such as Lamb shifts,[1] Van der Waals forces,[2] and Förster resonance energy transfer (FRET).[3] Recently, DDIs have emerged as an efficient approach for enabling long-range energy transfer,[4] collective superradiance and subradiance,[5] and the realization of superconducting qubits in circuit quantum electrodynamic (QED) systems.[6] These interactions can be understood as the process of virtual photon absorption and re-emission, determined by the interaction distance and coupling strength.[3]

Enabled by DDIs, FRET has been essential in fluorescence applications, including

biosensing,[7, 8] light harvesting,[9, 10] DNA analysis,[11] and optical imaging.[12] The widespread use of FRET stems from its optimal energy transfer distances, typically corresponding to the size of a protein or the thickness of a membrane, making it a gold standard in biomedical research.[13] Inherited from the DDI nature, FRET is a near-field phenomenon whose strength and length can be enhanced by modifying either molecular properties or the surrounding electromagnetic environment. For instance, one can improve the energy transfer efficiency by optimizing the orientation of the donor and acceptor molecules.[14] On the electromagnetic environment front, several approaches have been proposed to enhance energy transfer efficiency and interaction distance: (1) employing optical microcavities such as the Fabry-Perot cavity and Whispering-gallery mode cavities to confine photons;[15-23] (2) ultilizing nanoplasmonic systems to further confine light within the subwavelength regime (i.e., ultrasmall mode volume), significantly boosting the photonic local density of the state (LDOS);[24-26] and (3) leveraging plasmonic nanoparticle lattice, which offers a high Q-factor, and large spatial coherence due to the hybridization between the localized surface plasmon resonances (LSPR) with in-plane diffraction orders.[27-29]

It is important to note that the above approaches can also be employed to enhance spontaneous emission, as the LDOS can be increased by the micro-nanocavities or plasmonic lattice via Purcell effect. However, there is an ongoing debate about whether the FRET rate or efficiency can be improved solely by enhancing the LDOS within these cavities.[16] Interestingly, some studies suggest that FRET efficiency may not benefit from microcavity-induced LDOS enhancement.[16, 17] This is because the energy transfer process is primarily governed by the electromagnetic field generated by donor molecules at the position of acceptor molecules.[27] In addition, spontaneous emission from the donor serves as a competing pathway, which can further reduce FRET efficiency. Therefore, achieving high FRET efficiency and extended interaction distance requires not only effective light confinement (i.e., high Q-factor) but also a moderate Purcell factor.

The concept of bound-state in-the continuum (BIC) has recently emerged as a promising platform for various optoelectronic applications such as low-threshold lasing,[30-32] nonlinear optics,[33-35] Bose-Einstein condensation,[36-39], optical trapping and biosensing.[40-42] Theoretically, photons can be indefinitely trapped inside a BIC cavity (i.e., $Q \rightarrow \infty$) because the BIC states are completely decoupled from the radiation continuum. Moreover, the ultrahigh-Q of symmetry-protected BICs is extremely robust against fabrication imperfections as long as the overall symmetry is preserved. Compared to traditional micro-nanocavities, BIC cavities made of loss-less dielectric materials offer several advantages for improving FRET efficiency and interaction distance. These advantages include ultrahigh-Q factors, ultralow material absorption (in contrast to metallic plasmonic and surface plasmon lattice cavities), and larger mode volumes due to the non-local effect (resulting in smaller Purcell factor).

In this work, we demonstrate remarkable FRET enhancement and long-range interaction distance by leveraging the BIC concept in a loss-less dielectric metasurface at ambient conditions (Fig. 1a). By utilizing a specialized back focal plane (BFP) microspectrometer, we study both angle-resolved and spectral-resolved photoluminescence (PL) lifetimes of dye molecules in the FRET system. We observed that PL lifetime was reduced in both BIC (i.e., dark mode) and bright modes owing to the Purcell effect within the metasurface. Intriguingly, both the FRET efficiency and the interaction distance were significantly enhanced in the BIC

mode near normal incidence (i.e., quasi-BIC). Our findings strongly indicate that BIC cavities are highly suitable for boosting FRET and collective DDIs, paving the way for further applications in FRET biomolecular sensing and imaging, as well as long-range qubit interactions in circuit QED.

Fig. 1a shows how donor-acceptor pairs interact with a Bound State in the Continuum (BIC) cavity. This cavity is created by a sub-diffractive square array of dielectric resonators. The system's symmetrical design causes destructive interference among all resonators, resulting in the formation of the BIC when light incident the array at a normal angle. At BIC resonance, spontaneous emission from donor molecules is suppressed, while the energy transfer from donor to acceptor molecules is significantly enhanced. Rhodamine 6G (R6G) and Nile Red (NR) are chosen to be the donor and acceptor, respectively in our study because of the well-overlapping between R6G's emission and NR's absorption spectra (Fig. S1) which facilitating efficient FRET between them. The BIC cavity is constructed from a 50 × 50 μm^2 square array of titanium dioxide (TiO_2) nanoholes, as shown in the scanning electron microscope (SEM) image in Fig. 1b. The nanofabrication process is described in detail in the Methods section and Fig. S2. The nanostructures are made from TiO_2, a material with a relatively high refractive index (n ~2.4 at ~560 nm) and minimal loss in the visible wavelength range. These properties make TiO_2 an ideal choice for high-Q metasurfaces, which have been shown to support BIC modes arising from various sources, including vertical magnetic dipoles (MD_z), electric quadrupoles (EQ), and so on. Here we select the fundamental BIC mode (i.e., MD_z) to couple with the dye solution as it has good spatially and spectrally overlap with R6G. The top panel of Fig. 1c shows the circulating electrical field distribution in a unit cell of nanohole structure, indicating the vertical magnetic dipole nature of the BIC mode.

In FRET, the excess energy due to the relaxation of the donor emitter to a lower energy state is transferred to the acceptor emitter. In homogeneous environments, FRET scales as R^{-6}, where R is the distance between donor and acceptor, typically limited to less than ten nanometers. The energy transfer rate is proportional to $\left|\mathbf{n_A}\cdot\overleftrightarrow{\mathbf{G}}(\mathbf{r_D},\mathbf{r_A})\mathbf{n_D}\right|^2$, where $\mathbf{n_D}$ and $\mathbf{n_A}$ are the unit orientation vectors of the donor and acceptor dipoles, respectively; $\overleftrightarrow{\mathbf{G}}(\mathbf{r_D},\mathbf{r_A})$ represents the dyadic Green's function at the acceptor position, $\mathbf{r_A}$, induced by the donor at position $\mathbf{r_D}$. In Finite Element Method simulation, we use an electric dipole to model a donor molecule in the TiO_2 nanostructure and calculate its radiation power $P=\frac{\omega}{2}\mathrm{Im}\{\boldsymbol{\mu}_D^*\cdot\boldsymbol{E}_D(\boldsymbol{r}_D)\}$ by integrating the Poynting flux over a far-field surface.[43] The Purcell factor for the donor can be defined as P/P_0, where P_0 is the reference radiation power. By calculating the dyadic Green's function using a point probe at various distance ($\boldsymbol{r}_A$) to the dipole source, we can simulate the energy transfer rate from donor to acceptor[27] as $\Gamma_{ET}=\frac{\omega}{2}\mathrm{Im}\{\boldsymbol{\mu}_A^*\cdot\boldsymbol{E}_D(\boldsymbol{r}_A)\}=3/2\sqrt{\varepsilon_0/\mu_0}\,n(\omega_0)\sigma_A(\omega_0)\left|\boldsymbol{n}_A\cdot\boldsymbol{E}_D(\boldsymbol{r}_A)\right|^2$,[3] where σ_A is absorption cross section, and $n(\omega_0)$ is the refractive index. When the donor dipole is positioned at the

edge of the nanohole, the dipole-generated electric field extends across the entire array, resulting in the same order of $\boldsymbol{E_D(r_D)}$ and $\boldsymbol{E_D(r_A)}$ (Fig. S3). By simultaneously scanning the position of the donor and acceptor, the distribution of the Purcell factor and FRET efficiency enhancement can be mapped, as shown in the middle and bottom panels of Fig. 1c, respectively. It is noted that these results are averaged from different *z* planes (see Fig. S4 for details). According to the simulation results, after considering the different *z* locations and different donor dipole directions (x, y, and z), the average Purcell factor $\overline{F_p} = \iint_{x,y} F_p(x,y)/S$ and FRET rate enhancement $\overline{\Gamma_{ET}} = \iint_{x,y} \Gamma_{ET}(x,y)/S$ are calculated to be 30 and 2.7×10^6, respectively. The Purcell factor is significantly smaller than the FRET rate enhancement because the FRET rate without the cavity decreases rapidly as the distance between the donor and acceptor increases $\Gamma_0 = P_0 (R_0/R_{DA})^6$, while dipole energy dissipation rate *P* and FRET rate Γ maintain the same order of magnitude. Futhermore, Figs. 1d and 1e show the simulated wavelength-momentum dispersion and Q-factors-momentum dispersion of the BIC and bright modes. As moving away from the Γ point (i.e., normal incidence), the Q-factor decreases rapidly, indicating the symmetry-protected nature of the BIC.

We then conducted optical characterizations using a home-built BFP microspectrometer, as illustrated in Fig. 2a and in the Methods section. Fig. 2b shows the simulated angle-resolved absorption spectra of the TiO_2 nanohole array with thickness t = 342 nm, hole diameter D = 300 nm, and periodicity a = 320 nm using rigorous coupled wave analysis (RCWA) in Lumerical software. The simulated spectrum agrees well with the measured angle-resolved reflection spectra in Fig. 2c, where the symmetry-protected BIC resonance occurs around 564 nm at normal incidence (θ = 0°), indicated by the vanishing reflectance signal. Fig. 2d shows the angle-resolved PL spectra of the donor emitter without the presence of the acceptor in TiO_2 nanohole array, indicating good coupling with the photonic resonance modes. Both the bright mode and BIC mode exhibit significant PL enhancement, due to the Purcell and outcoupling effects with the exception at normal incidence in the BIC case due to the symmetry-protected nature.

To better discriminate the PL lifetime in each photonic mode, we add a movable pinhole at the BFP to collect the PL signal within a narrow angle range (Δθ ~ 1°). Fig. 2e presents the stitched PL spectra measured with different pinhole positions, showing a good agreement with the result without the pinhole as shown in the white dashed line box in Fig. 2d. The reflection and PL spectra for angles from 0° to 5° are shown in Fig. S5, where the bright mode exhibits a blue shift with increasing angle, while the BIC mode undergoes a redshift. Time-resolved PL measurements confirm that the exciton decay rate of the donor is enhanced by the photonic modes compared to the case without nanostructures (Fig. 2f). Given that the organic dye solution (~ 10 μm thick) is much thicker than the TiO_2 nanohole array (~ 342 nm), the PL signal from the uncoupled background emitters significantly contributes to the collected signals. To accurately analyze the PL lifetime associated with the photonic modes, we exploited a bi-exponential decay function to fit and analyze the PL lifetime for the on-resonance cases (resonance wavelength and angle) while using the single-exponential decay function for the

off-resonance cases (Fig. S6 and Table S1).The t2 value in the bi-exponential decay is comparable to the t1 value in the single-exponential decay, indicating that both arise from the uncoupled background PL. Consequently, a map of PL lifetime as a function of wavelength and angle can be obtained, as shown in Fig. 2g. The off-resonance PL also shows a slight increase in exciton decay rate, likely due to the TiO_2 structure which can accelerate the spontaneous emission rate of the emitters.[44]

We now study the FRET rate enhancement by characterizing the PL lifetime of the donor emitters with the presence of the acceptor molecules using the same BFP technique described above. The FRET rate can be written as $\Gamma_{ET} = 1/\tau_{DA} - 1/\tau_D$, where τ_{DA} and τ_D are the PL lifetime of donor emitters with and without acceptor, respectively. As shown in Fig. 3a, the maximum FRET rate enhancement reaches 63.8 near the normal incidence of the BIC mode (quasi-BIC), while the bright mode has almost no obvious FRET rate enhancements. Futhermore, we characterized the FRET rate for the donor-acceptor pairs coupled with BIC mode and on a blank substrate at various donor-acceptor distances, as illustrated in Fig. 3b. The donor-acceptor distances (i.e., mean N-N separation between the donor−acceptor pairs in the solution) were varied by changing the concentration of donor/acceptor and can be estimated as $R_{DA} = 1/2\sqrt[3]{C}$,[45] where C is the concentration of donor and acceptor. Without coupling to a photonic mode, the FRET rate decreases rapidly as the donor-acceptor distance increases, approaching zero when the distance exceeds 10 nm, in good agreement with the reports in the literature.[13] In contrast, when the donor-acceptor pairs are coupled with the BIC mode, the FRET rate decreases much more slowly with distance, resulting in a detectable FRET rate even at a donor-acceptor distance of 100 nm. FRET rate enhancements at different donor-acceptor distances for BIC resonance are plotted in Fig. 3c, where the FRET rate enhancement remains around 20 times even at a 100 nm donor-acceptor distance. To elucidate the mechanism of extended FRET distance, we present Figs. S7 and S8, which depict the distribution of the FRET rate when the donor dipole is positioned at the edge of the nanohole (showing strong spatial overlap with the MD_z BIC mode) and at the center of the nanohole (showing weak spatial overlap with the MD_z BIC mode). In Figure S7, when the donor dipole is situated at the location of the maximum electric field in the MD_z BIC mode, its generated electric field can extend to other nanoholes due to the nonlocal nature of the BIC mode. Furthermore, even when the donor is placed at the nanohole center, the electric field can still partially extend to other nanoholes (Fig. S8). Consequently, the dipole-dipole interaction distance is significantly increased. In addition, FRET efficiency (Φ_F), another essential parameter to characterize FRET, can be calculated as $\phi_F = 1 - \tau_{DA}/\tau_D$. Fig. S9 shows the FRET efficiency enhancement mapping and estimated donor-acceptor distance dependence of the FRET efficiency, with the maximum FRET efficiency enhancement reaching 18.8.

To better understand the underlying mechanism of BIC-coupled FRET, we first investigate the Purcell factor and FRET rate enhancement by varying the wavelength and momentum while maintaining a moderate distance of 20 nm between donor and acceptor as shown in Fig. 4a. The resulting Purcell factor and FRET rate enhancement maps are presented in Figs. 4b and 4c, respectively. These results agree well with the simulation shown in Fig. 1d, indicating that the

BIC mode is responsible for the FRET rate and Purcell enhancement. It is noted that, for the Purcell factor, the maximum value occurs at a small angle rather than the normal incidence (k = 0) because light can not couple to the BIC mode at this angle. In contrast, the FRET rate enhancement reaches the maximum at the normal incident angle and decays as the angle (momentum) increases, which can be attributed to the reduction in the Q-factor of the BIC mode. Additionally, the simulations of the Purcell factor and FRET rate enhancement for the bright mode, presented in Fig. S10, reveal that while the Purcell factor is higher in the bright mode, the FRET rate enhancement is relatively low. These simulation results agree well with the experimental observation shown in Fig. 3a, indicating that the BIC mode, rather than the bright mode, is essential in enhancing FRET efficiency.

Finally, we simulate the FRET rate enhancements by varying the donor-acceptor distance. In these simulations, the donor and acceptor molecules are positioned at the same x and y coordinates but are separated along z-direction with a distance R (Fig. 4d). As illustrated in Fig. 4e for the blank substrate case (black curve), the FRET rate decreases as the scale of $1/R^6$, which is consistent with theoretical expectations for FRET. Notably, the BIC mode exhibits a significantly higher FRET rate enhancement compared to both the substrate and the bright mode. This finding is corroborated by the experimental results shown in Fig. 3a, where the BIC mode has higher FRET rate enhancement than the bright mode. A particularly important observation is that the FRET rate in BIC mode decays extremely slowly at donor-acceptor distances below 200 nm. This result explains why a detectable FRET rate persists even at a 100 nm distance in our experiments as shown in Fig.3b. Fig. 4f further illustrates that FRET rate enhancement in the BIC mode reaches its maximum at a donor-acceptor distance of around 100 nm. Additionally, we also simulate the FRET rate when donor and acceptor molecules are separated in the xy-plane but positioned at the same z-coordinate (Fig. S11). In this scenario, the FRET rate enhancement peaks at around 70 nm separation distance. These results slightly differ from our experimental observation of ~ 30 nm shown in Fig. 3c, likely due to the experimental FRET rates on the substrate being overestimated compared to the theoretical calculation (Fig. S12).

In summary, we demonstrate a remarkable FRET rate enhancement and long-range dipole-dipole interaction in a mixed dye solution by coupling with a BIC mode in a dielectric metasurface cavity. Spectrally and angularly resolved PL lifetime studies reveal that the BIC mode significantly outperforms the bright mode in FRET rate enhancement (i.e., up to 70 times compared to off-resonance case), despite having only a moderate Purcell factor. Furthermore, we discovered that the FRET distance between donor and acceptor molecules in aqueous solution can be boosted more than 10 times (up to 100 nm) in our experiments and over 30 times (up to 300 nm) in our simulations. We anticipate that these enhanced and long-range interactions could serve not only as a powerful tool for studying biomolecular interactions and advancing biomedical imaging but also as a novel platform for quantum entanglement and long-range qubit interactions in circuit QED systems.

Supporting Information

Dye spectrum, details of sample fabrication, details of COMSOL calculation for FRET in BIC mode,details of COMSOL calculation for FRET in bright mode, details of time-resolved PL analysis, details of experimental FRET efficiency enhancement.

Methods

Numerical simulation

Simulations were carried out using the Finite Element Method (Comsol Multiphysics) and Rigorous Coupled Wave Analysis (RCWA) in the Lumerical. Bloch boundary conditions are applied to the unit cell in the lateral directions. The refractive index of substrate was selected as 1.46, corresponding to the quartz substrate. Meanwhile, the refractive index of the surrounding medium was chosen as 1.427, corresponding to Methanol: DMSO solution with volume ratio of 1:2 in the experiments.

Fabrication of dielectric nanostructures

We deposited a titanium dioxide (TiO_2) film with 340 nm thickness on a quartz substance by using ion-assisted deposition (IAD, Oxford Optofab300). Following this, we deposited a 30 nm chromium (Cr) film as a hard mask via electron-beam evaporation (Angstrom EvoVac). Then, we spin-coated hydrogen silsesquioxane (HSQ) as a negative electron-beam resist on the TiO2/Cr/quartz sample (2×2 cm^2) at 5000 rpm for 60 seconds and then baked on a hotplate at 180 °C for 3 minutes. Subsequently, we patterned the HSQ using electron beam lithography (EBL, Elionix ELS 7000), and used a mixture of 1 wt.% NaOH and 4 wt.% NaCl in deionized water to develop the sample in 4 minutes, followed by a rinse with deionized (DI) water. After the inductively coupled plasma reactive ion etching (ICP-RIE, Oxford Plasmalab 100) with a gas mixture of Cl_2 at 15 sccm and O_2, maintained at 10 mTorr and 7 °C, the EBL-written patterns was transferred to the Cr layer. Subsequently, the patterns on the Cr layer were etched into the TiO_2 layer by using CHF_3 gas in the same ICP-RIE system, operating at 19 sccm, 27 mTorr, and 20 °C. Lastly, we used the chromium etchant (Merck) solution to remove the remaining Cr, which was rinsed with DI water and blow-dried with nitrogen gas.

Dye solution preparation

Rhodamine 6G and Nile Red were purchased from Sigma-Aldrich (Product IDs #R4127 and #72485, respectively). The dye molecule solutions are prepared in methanol and DMSO with a volume ratio of 1:2. These stock solutions have a donor and acceptor dye concentration (C) of 1 mM. The average donor-acceptor distance can be estimated as 5.9 nm. We can increase the donor-acceptor distance by diluting the stock dye solution. In particular, the donor-acceptor distances can be adjusted to 10 nm, 13 nm, 22 nm, 34 nm, 43 nm, 60 nm, and 100 nm, by diluting the stock solution with the factors of 5, 10, 50, 200, 400, 1000, and 5000, respectively.

Optical characterizations

Optical characterizations were performed with a home-built microspectrometer. The setup consists of an inverted optical microscope (Nikon Ti-U), a spectrometer (Andor SR-303i), and an electron-multiplying charge-coupled detector (EMCCD, Andor Newton 971). To measure reflectance, the white light was guided in the microscope system to excite the sample surface by using a 20× objective (NA = 0.4). The same objective collected the reflected light and

directed it through lenses and a polarizer, which focused the objective's back focal plane (BFP) onto the spectrometer's entrance slit. The slit width was adjusted to 100 μm to isolate a narrow portion of the BFP image, capturing light reflected from the sample specifically in the *yz*-plane. A grating with 150 lines/mm was employed to disperse the light by wavelength. Then, the CCD within the spectrometer provides the reflection spectra, resolved by wavelength and reflection angle in the two-dimensional *yz*-plane.

For photoluminescence (PL) measurements, excitation light from a supercontinuum laser (NKT SuperK) at $\lambda = 488$ nm (pulse width = ~ 7ps, repetition rate = 80 MHz) was focused onto the sample through a 10× objective (NA = 0.3). Following, PL emitted by the sample was received by a 20× objective (NA = 0.4). In both reflection and PL measurements, collected signals were passed through a long-pass filter and a linear polarizer (for s-polarization). For PL lifetime measurements, the avalanche photodiode (APD) (Excelitas Technologies) collected the PL signal after passing through the small pinhole at BFP and the narrow slit behind the grating.

Acknowledgements

S.T.H, T.T.H.D, and V.V acknowledge funding support from Singapore MTC Programmatic administered by A*STAR (Grant No. M21J9b0085). C. D, Z. Y, and Y. W. acknowledge funding support from the National Research Foundation Competitive Research Program (NRF-CRP29-2022-0003), Ministry of Education, Singapore, under its AcRF Tier 2 grant (MOE-T2EP50121-0012) and AcRF Tier 1 grant (RG140/23). H.S.N acknowledges funding support from the French National Research Agency under the project POLAROID (ANR-24-CE24-7616-01).

Author contributions

C.D., S.T.H., and Z.Y. conceived the idea. Z.Y. performed the numerical simulations and theoretical analysis, fabricated the samples, measured reflectance, measured PL lifetimes, prepared the figures and wrote the manuscript. Y.W. and T.T.H.D., helped to fabricate the samples. V.V. characterised the nanostructures. C.S. and H.S.N. performed the theoretical analysis. N.N. and Y.-C. C. provided the organic dye solutions. C.D. and S.T.H. supervised the project.

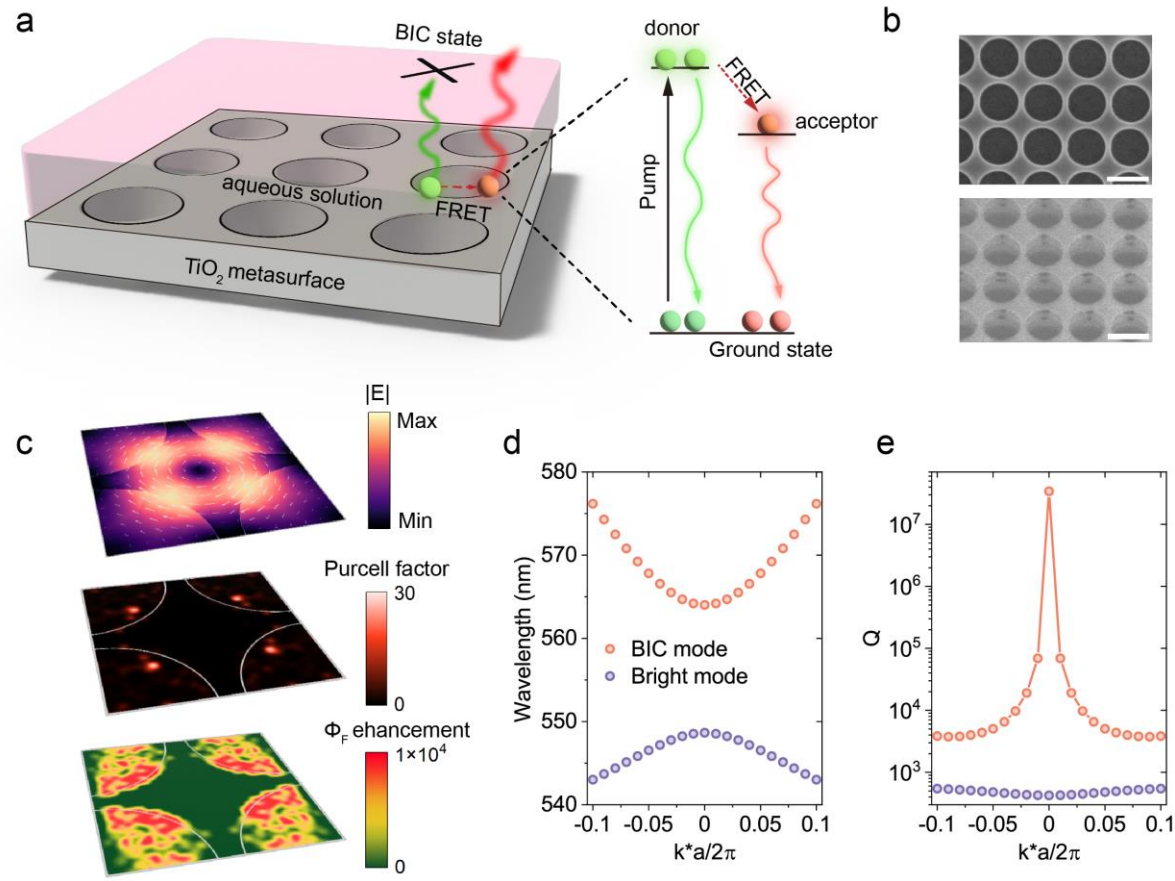

Figure 1. (a) The schematic of the FRET enhancement in mixed-dyes solution by TiO_2 nanohole array supporting bound-state in-the continuum (BIC). **(b)** Scanning electron microscope (SEM) images of the top view (upper panel) and 30° tilted view (lower panel) of the fabricated TiO_2 nanohole array. Scale bars are 300 nm. **(c)** Electric-field distribution (top), in-plane dipole Purcell factor distribution (middle), and in-plane dipole FRET efficiency (Φ_F) enhancement distribution (bottom) at the BIC frequency in the nanohole array. The Purcell factor and FRET efficiency enhancement out of nanohole are set to 0 because the dipoles can only exist within the nanohole. **(d)** Simulated wavelength-momentum dispersion of BIC mode (dark mode) and bright mode for s-polarization. **(e)** Simulated Q-factors-momentum dispersion of the modes in **(d)**.

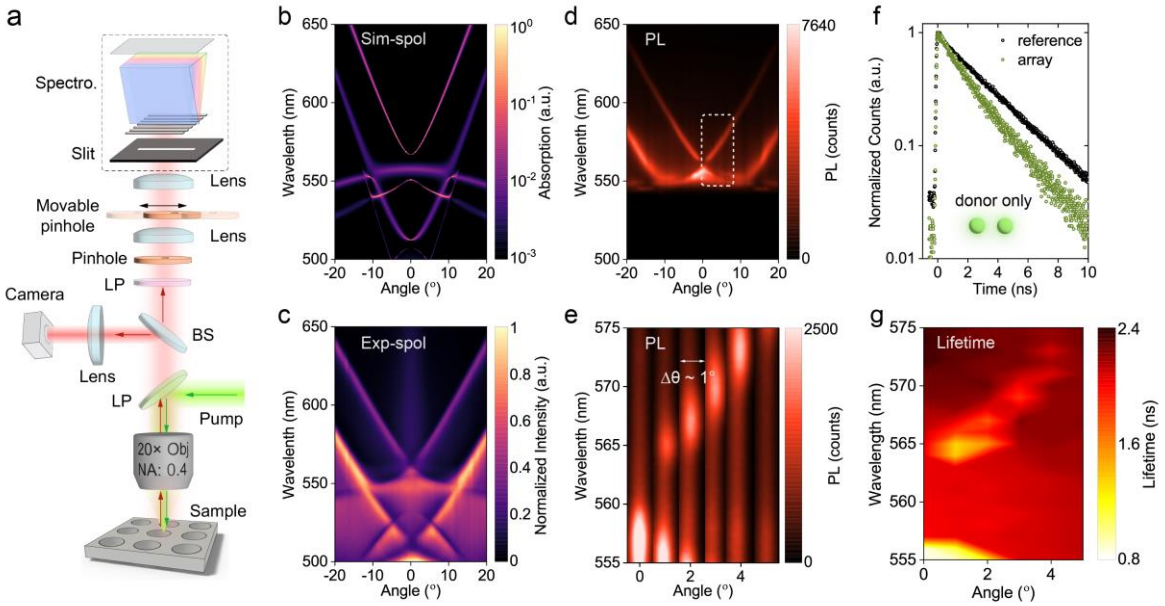

Figure 2. (a) Schematic of the spectrally resolved back focal plane (BFP) microspectrometer setup used for optical characterizations. BS: beam-splitter, LP: long-pass filter, Spectro: spectrometer. **(b)** Simulated angle-resolved absorption spectra of the designed TiO_2 nanohole array, showing vertical magnetic dipole BIC resonance ~ 564 nm at normal incidence (Angle = 0°). **(c)** Measured angle-resolved reflectance spectra. **(d)** Angle-resolved PL spectra of organic dye coupled with the TiO_2 nanohole array showing PL enhancement of the modes. **(e)** Stiched angle-resolved PL spectra after adding a movable pinhole at the BFP. In this case, the angle step, corresponding with the movement of the pinhole, is $\Delta\theta \sim 1°$. **(f)** Extracted time-resolved PL of the donor dye with and without TiO_2 nanohole array. **(g)** Mapping of experimental PL lifetime versus wavelength and angle. All optical characterization data (both simulation and experiment) shown here are for s-polarization.

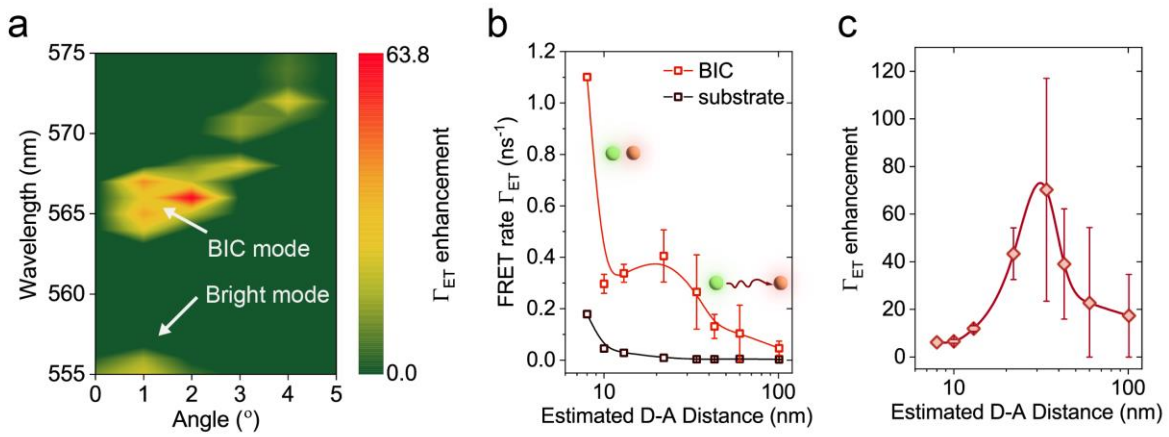

Figure 3. (a) Dependence of measured FRET rate enhancement (i.e., the ratio between the FRET rate with and without TiO_2 nanohole array) on wavelength and collection angle. Here, FRET rate is defined as $\Gamma_{ET} = 1/\tau_{DA} - 1/\tau_D$. **(b)** Estimated D-A distance dependence of the FRET rate Γ_{ET} at BIC resonance and on the substrate. FRET rates at BIC resonance were extracted from wavelength ~ 566nm and collection angle ~ 1°. **(c)** Estimated D-A distance dependence of the FRET rate enhancement at BIC resonance.

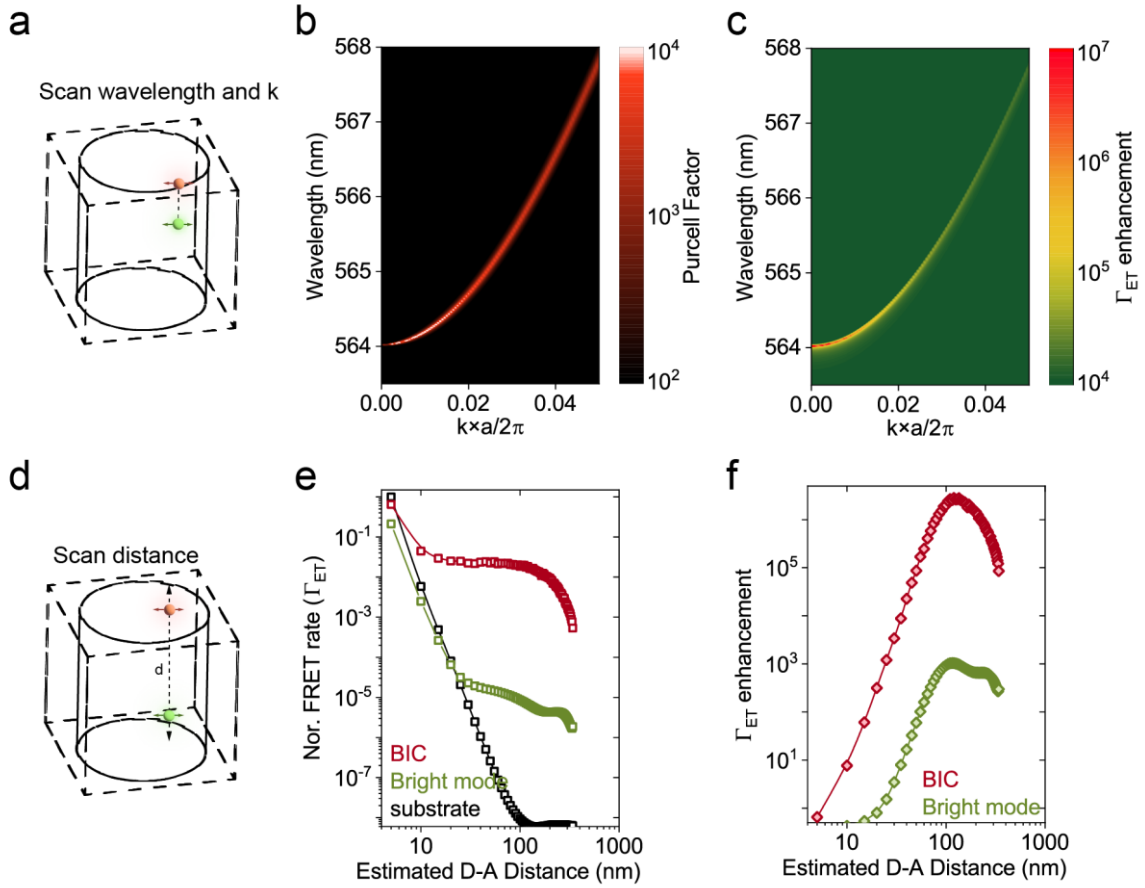

Figure 4. **(a)** Schematic of the wavelength- and k-scan dipole-dipole simulation in b and c where the distance of donor and acceptor is fixed at 20 nm. **(b)** Simulated Purcell factor (**b**) and FRET rate enhancement (**c**)dependence on wavelength and k. **(d)** Schematic of the z-scan dipole-dipole simulation where positions of donor and acceptor in *xy*-plane are fixed. **(e)** D-A distance dependence of the FRET rate, $\Gamma_{ET,}$ under the BIC mode, bright mode, and substrate. **(f)** D-A distance dependence of the FRET rate enhancement under the BIC mode and bright mode.

References:

(1) Hutson, R. B.; Milner, W. R.; Yan, L.; Ye, J.; Sanner, C. Observation of millihertz-level cooperative Lamb shifts in an optical atomic clock. *Science* **2024**, *383*, 384-387.

(2) Kamenski, A.; Manakov, N.; Mokhnenko, S.; Ovsiannikov, V. Energy of van der Waals and dipole-dipole interactions between atoms in Rydberg states. *Phys. Rev. A* **2017**, *96*, 032716.

(3) Novotny, L.; Hecht, B. *Principles of nano-optics*; Cambridge university press, 2012.

(4) Deshmukh, R.; Biehs, S.-A.; Khwaja, E.; Galfsky, T.; Agarwal, G. S.; Menon, V. M. Long-range resonant energy transfer using optical topological transitions in metamaterials. *ACS Photonics* **2018**, *5*, 2737-2741.

(5) Tiranov, A.; Angelopoulou, V.; van Diepen, C. J.; Schrinski, B.; Sandberg, O. A. D. A.; Wang, Y.; Midolo, L.; Scholz, S.; Wieck, A. D.; Ludwig, A.; Sørensen, A. S.; Lodahl, P. Collective super-and subradiant dynamics between distant optical quantum emitters. *Science* **2023**, *379*, 389-393.

(6) Van Loo, A. F.; Fedorov, A.; Lalumiere, K.; Sanders, B. C.; Blais, A.; Wallraff, A. Photon-mediated interactions between distant artificial atoms. *Science* **2013**, *342*, 1494-1496.

(7) Yuan, Z.; Tan, X.; Gong, X.; Gong, C.; Cheng, X.; Feng, S.; Fan, X.; Chen, Y.-C. Bioresponsive microlasers with tunable lasing wavelength. *Nanoscale* **2021**, *13*, 1608-1615.

(8) Wang, Z.; Fang, G.; Gao, Z.; Liao, Y.; Gong, C.; Kim, M.; Chang, G.-E.; Feng, S.; Xu, T.; Liu, T.; Chen, Y.-C. Autonomous microlasers for profiling extracellular vesicles from cancer spheroids. *Nano Lett.* **2023**, *23*, 2502-2510.

(9) Yuan, Z.; Wang, Z.; Guan, P.; Wu, X.; Chen, Y. C. Lasing-encoded microsensor driven by interfacial cavity resonance energy transfer. *Adv. Opt. Mater.* **2020**, *8*, 1901596.

(10) Yu, J.; Sharma, M.; Sharma, A.; Delikanli, S.; Volkan Demir, H.; Dang, C. All-optical control of exciton flow in a colloidal quantum well complex. *Light Sci. Appl.* **2020**, *9*, 27.

(11) Yun, C.; Javier, A.; Jennings, T.; Fisher, M.; Hira, S.; Peterson, S.; Hopkins, B.; Reich, N.; Strouse, G. Nanometal surface energy transfer in optical rulers, breaking the FRET barrier. *J. Am. Chem. Soc.* **2005**, *127*, 3115-3119.

(12) Kamino, K.; Kadakia, N.; Avgidis, F.; Liu, Z.-X.; Aoki, K.; Shimizu, T. S.; Emonet, T. Optimal inference of molecular interaction dynamics in FRET microscopy. *Proc. Nat. Acad. Sci.* **2023**, *120*, e2211807120.

(13) Lakowicz, J. Principles of Fluorescence Spectroscopy. *University of Maryland School of Medicine Baltimore* **2006**, *132*.

(14) Erdem, O.; Gungor, K.; Guzelturk, B.; Tanriover, I.; Sak, M.; Olutas, M.; Dede, D.; Kelestemur, Y.; Demir, H. V. Orientation-controlled nonradiative energy transfer to colloidal nanoplatelets: engineering dipole orientation factor. *Nano Lett.* **2019**, *19*, 4297-4305.

(15) Andrew, P.; Barnes, W. L. Forster energy transfer in an optical microcavity. *Science* **2000**, *290*, 785-788.

(16) Blum, C.; Zijlstra, N.; Lagendijk, A.; Wubs, M.; Mosk, A. P.; Subramaniam, V.; Vos, W. L. Nanophotonic control of the Förster resonance energy transfer efficiency. *Phys. Rev. Lett.* **2012**, *109*, 203601.

(17) Konrad, A.; Metzger, M.; Kern, A. M.; Brecht, M.; Meixner, A. J. Controlling the dynamics of Förster resonance energy transfer inside a tunable sub-wavelength Fabry–Pérot-resonator. *Nanoscale* **2015**, *7*, 10204-10209.

(18) Kushida, S.; Braam, D.; Dao, T. D.; Saito, H.; Shibasaki, K.; Ishii, S.; Nagao, T.; Saeki, A.; Kuwabara, J.; Kanbara, T. Conjugated polymer blend microspheres for efficient, long-range light

energy transfer. *ACS Nano* **2016**, *10*, 5543-5549.
(19) Jana, S.; Xu, X.; Klymchenko, A.; Reisch, A.; Pons, T. Microcavity-enhanced fluorescence energy transfer from quantum dot excited whispering gallery modes to acceptor dye nanoparticles. *ACS Nano* **2020**, *15*, 1445-1453.
(20) Zhou, Y.; Yuan, Z.; Gong, X.; Birowosuto, M. D.; Dang, C.; Chen, Y.-C. Dynamic photonic barcodes for molecular detection based on cavity-enhanced energy transfer. *Adv. Photonics* **2020**, *2*, 066002-066002.
(21) Coles, D. M.; Somaschi, N.; Michetti, P.; Clark, C.; Lagoudakis, P. G.; Savvidis, P. G.; Lidzey, D. G. Polariton-mediated energy transfer between organic dyes in a strongly coupled optical microcavity. *Nat. Mater.* **2014**, *13*, 712-719.
(22) Zhong, X.; Chervy, T.; Zhang, L.; Thomas, A.; George, J.; Genet, C.; Hutchison, J. A.; Ebbesen, T. W. Energy transfer between spatially separated entangled molecules. *Angew. Chem.* **2017**, *129*, 9162-9166.
(23) Sandik, G.; Feist, J.; García-Vidal, F. J.; Schwartz, T. Cavity-enhanced energy transport in molecular systems. *Nat. Mater.* **2024**, 1-12.
(24) Zambrana-Puyalto, X.; Maccaferri, N.; Ponzellini, P.; Giovannini, G.; De Angelis, F.; Garoli, D. Site-selective functionalization of plasmonic nanopores for enhanced fluorescence emission rate and Förster resonance energy transfer. *Nanoscale Adv.* **2019**, *1*, 2454-2461.
(25) Baibakov, M.; Patra, S.; Claude, J.-B.; Moreau, A.; Lumeau, J.; Wenger, J. Extending single-molecule Forster resonance energy transfer (FRET) Range beyond 10 nanometers in zero-mode waveguides. *ACS Nano* **2019**, *13*, 8469-8480.
(26) Ghenuche, P.; Mivelle, M.; de Torres, J.; Moparthi, S. B.; Rigneault, H.; Van Hulst, N. F.; García-Parajó, M. F.; Wenger, J. Matching nanoantenna field confinement to FRET distances enhances Forster energy transfer rates. *Nano Lett.* **2015**, *15*, 6193-6201.
(27) Boddeti, A. K.; Guan, J.; Sentz, T.; Juarez, X.; Newman, W.; Cortes, C.; Odom, T. W.; Jacob, Z. Long-range dipole–dipole interactions in a plasmonic lattice. *Nano Lett.* **2021**, *22*, 22-28.
(28) Newman, W. D.; Cortes, C. L.; Afshar, A.; Cadien, K.; Meldrum, A.; Fedosejevs, R.; Jacob, Z. Observation of long-range dipole-dipole interactions in hyperbolic metamaterials. *Sci. Adv.* **2018**, *4*, eaar5278.
(29) Boddeti, A. K.; Wang, Y.; Juarez, X. G.; Boltasseva, A.; Odom, T. W.; Shalaev, V.; Alaeian, H.; Jacob, Z. Reducing Effective System Dimensionality with Long-Range Collective Dipole-Dipole Interactions. *Phys. Rev. Lett.* **2024**, *132*, 173803.
(30) Ha, S. T.; Fu, Y. H.; Emani, N. K.; Pan, Z.; Bakker, R. M.; Paniagua-Domínguez, R.; Kuznetsov, A. I. Directional lasing in resonant semiconductor nanoantenna arrays. *Nat. Nanotechnol.* **2018**, *13*, 1042-1047.
(31) Hwang, M.-S.; Lee, H.-C.; Kim, K.-H.; Jeong, K.-Y.; Kwon, S.-H.; Koshelev, K.; Kivshar, Y.; Park, H.-G. Ultralow-threshold laser using super-bound states in the continuum. *Nat. Commun.* **2021**, *12*, 4135.
(32) Kodigala, A.; Lepetit, T.; Gu, Q.; Bahari, B.; Fainman, Y.; Kanté, B. Lasing action from photonic bound states in continuum. *Nature* **2017**, *541*, 196-199.
(33) Koshelev, K.; Kruk, S.; Melik-Gaykazyan, E.; Choi, J.-H.; Bogdanov, A.; Park, H.-G.; Kivshar, Y. Subwavelength dielectric resonators for nonlinear nanophotonics. *Science* **2020**, *367*, 288-292.
(34) Anthur, A. P.; Zhang, H.; Paniagua-Dominguez, R.; Kalashnikov, D. A.; Ha, S. T.; Maß, T. W.; Kuznetsov, A. I.; Krivitsky, L. Continuous wave second harmonic generation enabled by quasi-bound-

states in the continuum on gallium phosphide metasurfaces. *Nano Lett.* **2020**, *20*, 8745-8751.
(35) Lubin, G.; Oron, D.; Rossman, U.; Tenne, R.; Yallapragada, V. J. Photon correlations in spectroscopy and microscopy. *ACS Photonics* **2022**, *9*, 2891-2904.
(36) Ardizzone, V.; Riminucci, F.; Zanotti, S.; Gianfrate, A.; Efthymiou-Tsironi, M.; Suàrez-Forero, D.; Todisco, F.; De Giorgi, M.; Trypogeorgos, D.; Gigli, G.; Baldwin, K.; Pfeiffer, L.; Ballarini, D.; Nguyen, H. S.; Gerace, D.; Sanvitto, D. Polariton Bose–Einstein condensate from a bound state in the continuum. *Nature* **2022**, *605*, 447-452.
(37) Gianfrate, A.; Sigurðsson, H.; Ardizzone, V.; Nguyen, H. C.; Riminucci, F.; Efthymiou-Tsironi, M.; Baldwin, K. W.; Pfeiffer, L. N.; Trypogeorgos, D.; De Giorgi, M.; Ballarini, D.; Nguyen, H. S.; Sanvitto, D. Reconfigurable quantum fluid molecules of bound states in the continuum. *Nat. Phys.* **2024**, *20*, 61-67.
(38) Do, T. T. H.; Nonahal, M.; Li, C.; Valuckas, V.; Tan, H. H.; Kuznetsov, A. I.; Nguyen, H. S.; Aharonovich, I.; Ha, S. T. Room-temperature strong coupling in a single-photon emitter-metasurface system. *Nat. Commun.* **2024**, *15*, 2281.
(39) Wu, X.; Zhang, S.; Song, J.; Deng, X.; Du, W.; Zeng, X.; Zhang, Y.; Zhang, Z.; Chen, Y.; Wang, Y. Exciton polariton condensation from bound states in the continuum at room temperature. *Nat. Commun.* **2024**, *15*, 3345.
(40) Tittl, A.; Leitis, A.; Liu, M.; Yesilkoy, F.; Choi, D.-Y.; Neshev, D. N.; Kivshar, Y. S.; Altug, H. Imaging-based molecular barcoding with pixelated dielectric metasurfaces. *Science* **2018**, *360*, 1105-1109.
(41) Yesilkoy, F.; Arvelo, E. R.; Jahani, Y.; Liu, M.; Tittl, A.; Cevher, V.; Kivshar, Y.; Altug, H. Ultrasensitive hyperspectral imaging and biodetection enabled by dielectric metasurfaces. *Nat. Photonics* **2019**, *13*, 390-396.
(42) Hu, J.; Safir, F.; Chang, K.; Dagli, S.; Balch, H. B.; Abendroth, J. M.; Dixon, J.; Moradifar, P.; Dolia, V.; Sahoo, M. K. Rapid genetic screening with high quality factor metasurfaces. *Nat. Commun.* **2023**, *14*, 4486.
(43) Meng, Y.; Huang, D.; Li, H.; Feng, X.; Li, F.; Liang, Q.; Ma, T.; Han, J.; Tang, J.; Chen, G. Bright single-nanocrystal upconversion at sub 0.5 W cm−2 irradiance via coupling to single nanocavity mode. *Nat. Photonics* **2023**, *17*, 73-81.
(44) Karaveli, S.; Zia, R. Strong enhancement of magnetic dipole emission in a multilevel electronic system. *Opt. Lett.* **2010**, *35*, 3318-3320.
(45) Pieper, A.; Hohgardt, M.; Willich, M.; Gacek, D. A.; Hafi, N.; Pfennig, D.; Albrecht, A.; Walla, P. J. Biomimetic light-harvesting funnels for re-directioning of diffuse light. *Nat. Commun.* **2018**, *9*, 666.

TOC Graphic:

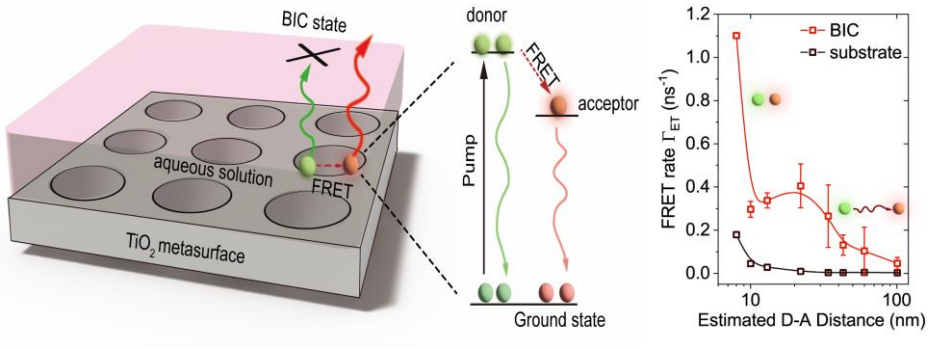
BIC state
aqueous solution
FRET
TiO_2 metasurface
donor
FRET
acceptor
Pump
Ground state
BIC
substrate
FRET rate Γ_{ET} (ns^{-1})
1.2
1.0
0.8
0.6
0.4
0.2
0.0
10
100
Estimated D-A Distance (nm)

Supporting Information for

Unleashing Giant Förster Resonance Energy Transfer by Bound State in The Continuum

Zhiyi Yuan[1,2,3], Ningyuan Nie[1], Yuhao Wang[1], Thi Thu Ha Do[3], Vytautas Valuckas[3], Christian Seassal[4], Yu-Cheng Chen[1], Hai Son Nguyen[4,5], Son Tung Ha[3,*], Cuong Dang[1,2,*]

[1] Centre for OptoElectronics and Biophotonics (COEB), School of Electrical and Electronic Engineering, Nanyang Technological University, Singapore 639798

[2] CNRS-International-NTU-Thales Research Alliance (CINTRA), IRL 3288, Singapore 637553

[3] Institute of Materials Research and Engineering, Agency for Science Technology and Research (A*STAR), 2 Fusionopolis Way, Singapore 138634

[4] Univ Lyon, Ecole Centrale de Lyon, CNRS, INSA Lyon, Universite Claude Bernard Lyon 1, CPE Lyon, CNRS, INL, UMR5270, 69130 Ecully, France

[5] Institut Universitaire de France (IUF), F-75231 Paris, France

*Corresponding authors: Son Tung Ha: ha_son_tung@imre.a-star.edu.sg & Cuong Dang: hcdang@ntu.edu.sg

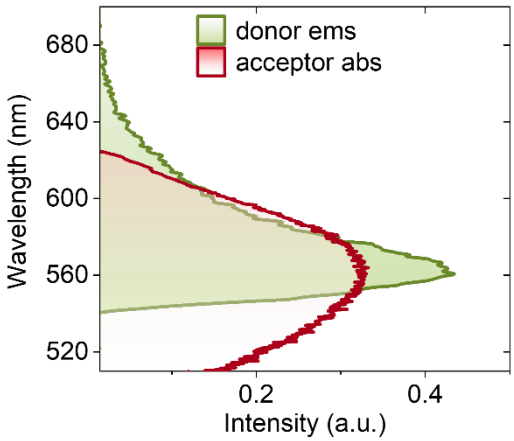

Fig. S1 Absorption and emission spectra from acceptor (Nile Red) and donor (R6G), respectively.

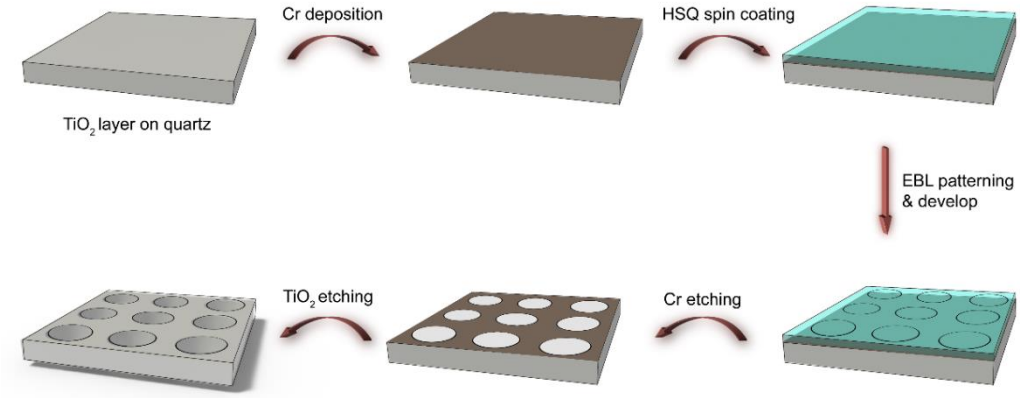

Fig. S2 Dielectric nanostructures fabrication process.

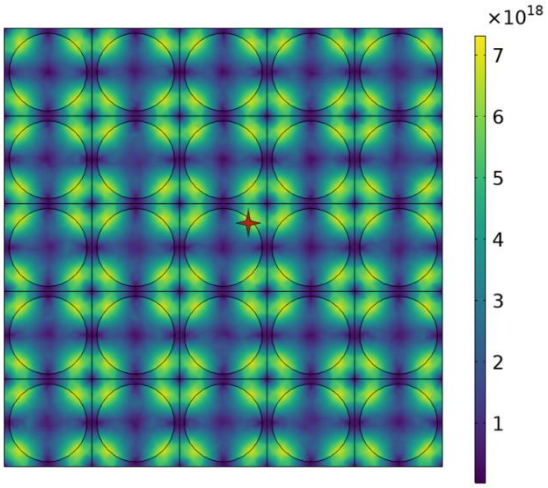

Fig. S3. *xy*-plane view of the single *y*-direction dipole-generated **electric field (E)** at the hole edge (labeled as a red star) of 5×5 unit cells array with periodic boundary.

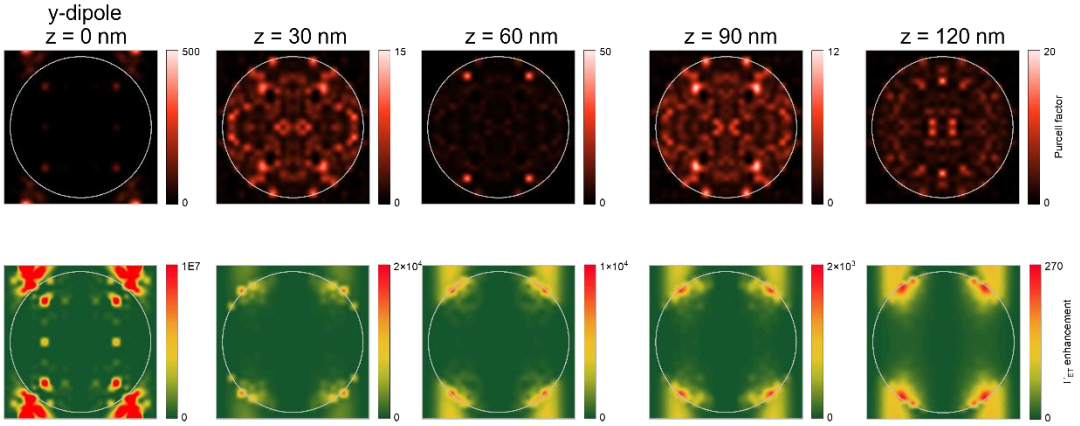

Fig. S4 Top view of the *y*-direction dipole Purcell factor and FRET rate enhancement distribution at the BIC frequency, at different *z*-axis positions. Here, we plot the Purcell factor and FRET rate enhancement distribution at several different *z*-axis. The *z*-averaged Purcell factor and FRET rate enhancement distribution are plotted in the maintext Fig. 1c. Then, after considering the different z locations (z = 0nm, 30nm, 60nm, 90nm, 120nm) and different donor dipole directions (x, y, and z), the averaged Purcell factor and FRET rate enhancement can be estimated by averaging the xy-position, z-position, and dipole-direction inside the nanohole: $F_p = \iint_{x,y} F_p(x,y)/S$. As such, the averaged Purcell factor $\langle F_p \rangle$ and FRET rate enhancement are 30 and 2.7×10^6 for the *y*-direction dipole.

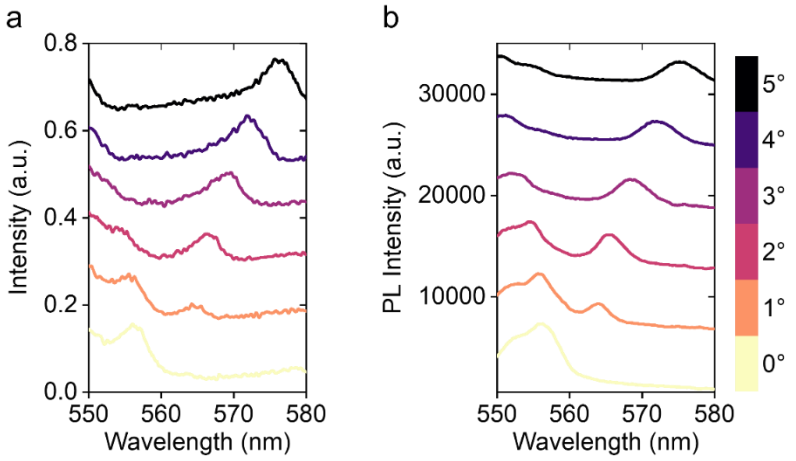

Fig. S5 (a) Reflection spectra at different incident angles of organic dye coupled TiO_2 nanohole array. **(b)** PL spectra at different incident angles of organic dye coupled TiO_2 nanohole array.

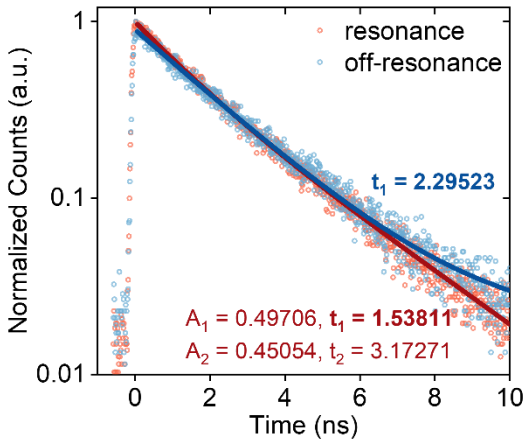

Fig. S6 Example time-resolved PL spectrum of organic dye coupled TiO_2 nanohole array at resonance situation (wavelength and angle) and off-resonance situation.

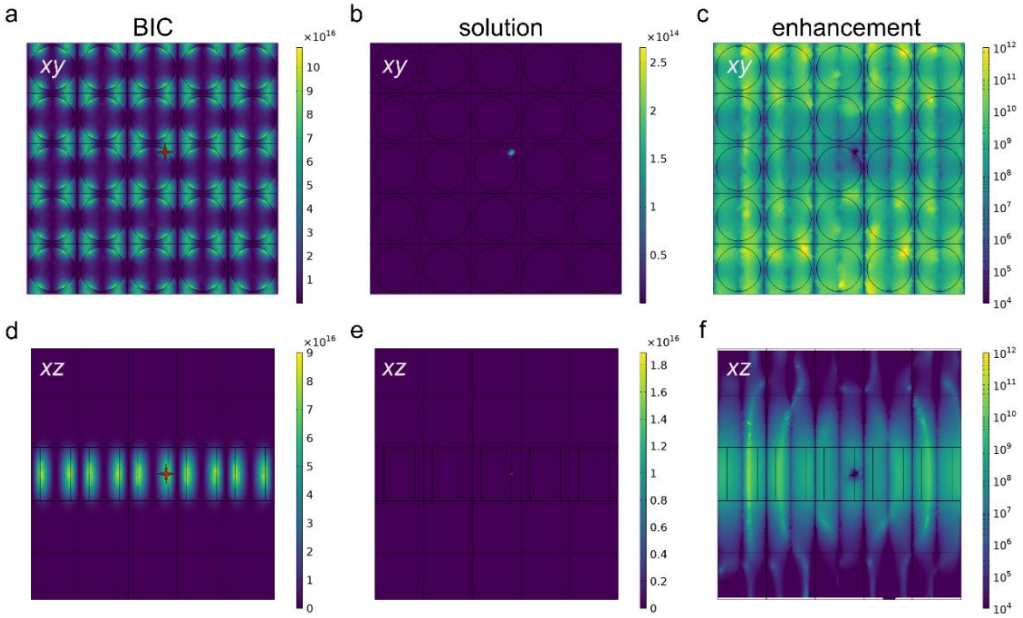

Fig. S7. (a-c) *xy*-plane view of the *y*-direction dipole at the hole edge (labeled as a red star) of 5×5 unit cells array with periodic boundary **(a)** FRET rate distribution in BIC mode. **(b)** FRET rate distribution in solution. **(c)** FRET rate enhancement distribution. **(d-f)** *xz*-plane view of the *y*-direction dipole **(d)** FRET rate distribution in BIC mode. **(e)** FRET rate distribution in solution. **(f)** FRET rate enhancement distribution.

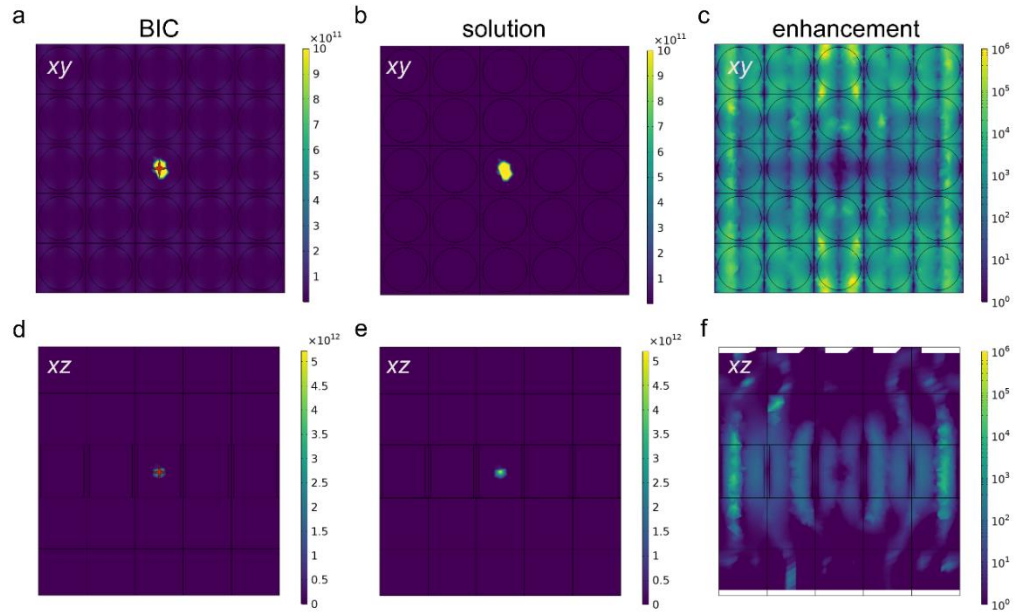

Fig. S8. (a-c) *xy*-plane view of the *y*-direction dipole at the hole center (labeled as a red star) of 5×5 unit cells array with periodic boundary **(a)** FRET rate distribution in BIC mode. **(b)** FRET rate distribution in solution. **(c)** FRET rate enhancement distribution. **(d-f)** *xz*-plane view of the *y*-direction dipole **(d)** FRET rate distribution in BIC mode. **(e)** FRET rate distribution in solution. **(f)** FRET rate enhancement distribution.

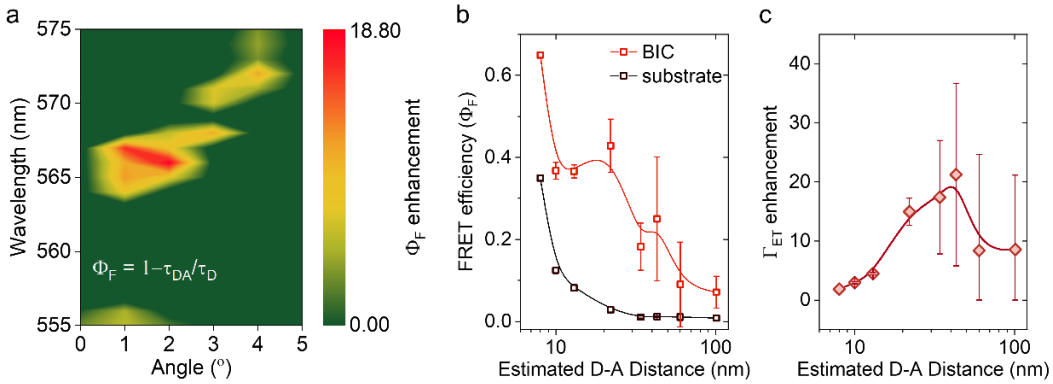

Fig. S9. (a) Mapping of experimental FRET efficiency enhancement (ratio between the FRET rate with and without TiO_2 nanohole array) versus wavelength and angle. FRET efficiency: $\phi_F = 1 - \tau_{DA}/\tau_D$. **(b)** Estimated D-A distance dependence of the FRET efficiency ϕ_F at BIC resonance and on the substrate. FRET efficiencies at BIC resonance were extracted from wavelength ~ 566nm, angle ~ 1°. **(c)** Estimated D-A distance dependence of the FRET efficiency enhancement at BIC resonance.

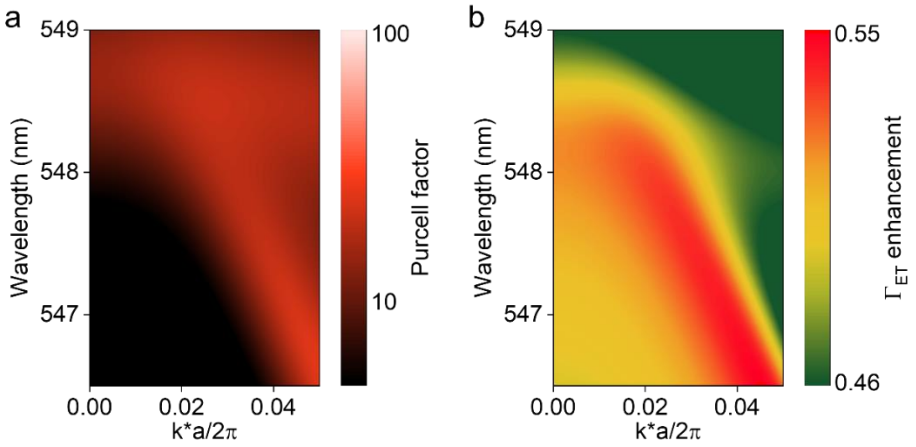

Fig. S10 (a) Mapping of simulated Purcell factor versus wavelength and k. **(b)** Mapping of simulated FRET rate enhancement versus wavelength and k.

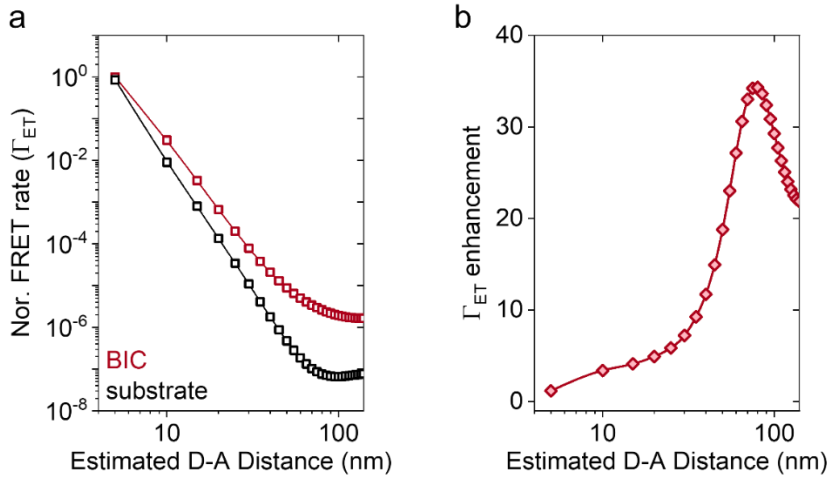

Fig. S11 (a) D-A distance dependence in *xy*-plane of the FRET rate Γ_{ET} under the BIC mode and substrate. **(b)** D-A distance dependence in *xy*-plane of the FRET rate enhancement under the BIC mode.

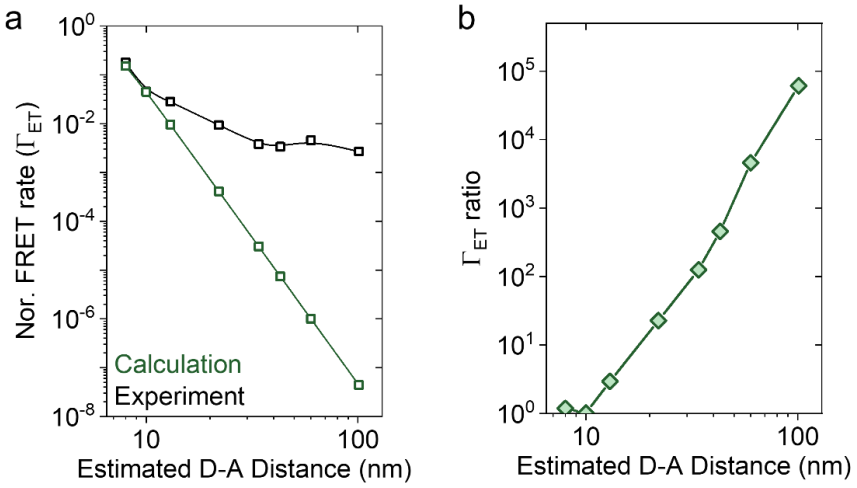

Fig. S12 (a) D-A distance dependence of the FRET rate Γ_{ET} in the solution (substrate) under experiment and calculation. **(b)** D-A distance dependence of the FRET rate ratio between the calculation and experiment.

On-resonance wavelength & angle	Off-resonance wavelength & angle	On-resonance wavelength & angle	Off-resonance wavelength & angle	On-resonance wavelength & angle	Off-resonance wavelength & angle
bi-exponential : A1	bi-exponential : t1	bi-exponential : A1	bi-exponential : t1	bi-exponential : A1	bi-exponential : t1
0.217	0.84	0.217	0.84	0.217	0.84
0.237	0.87	0.237	0.87	0.237	0.87
0.175	0.89	0.175	0.89	0.175	0.89
0.323	1.12	0.323	1.12	0.323	1.12
0.330	1.21	0.330	1.21	0.330	1.21

Table S1 Representative bi-exponential decay parameters from resonance situation and single-exponential decay parameters from off-resonance situation. For the bi-exponential decay, A1 and A2 are in the same order of magnitude, indicating the PL from resonance and background both play an important role in the signal. The t2 in bi-exponential decay is similar to the t1 in single-exponential decay, indicating both originated from the uncoupled background PL.